Bioactive Materials 43 (2025) 240–254

Contents lists available at ScienceDirect

Bioactive Materials

journal homepage: www.keaipublishing.com/en/journals/bioactive-materials

MMP-9 responsive hydrogel promotes diabetic wound healing by suppressing ferroptosis of endothelial cells

Chuanlu Lin [a,b,1], Yiqiang Hu [a,b,1], Ze Lin [a,b,1], Longyu Du [a,b,1], Yixin Hu [c], Lizhi Ouyang [a,b], Xudong Xie [a,b], Peng Cheng [a,b], Jiewen Liao [a,b], Li Lu [a,b], Ruiyin Zeng [a,b], Ping Xia [d,****], Zhiyong Hou [e,f,***], Guohui Liu [a,b,**], Hankun Hu [g,h,i,*]

[a] Department of Orthopedics, Union Hospital, Tongji Medical College, Huazhong University of Science and Technology, Wuhan, 430022, China
[b] Hubei Province Key Laboratory of Oral and Maxillofacial Development and Regeneration, Wuhan, 430022, China
[c] School of Pharmaceutical Sciences, Wuhan University, Wuhan, 430071, China
[d] Department of Orthopaedics, Wuhan Fourth Hospital (Puai Hospital), Wuhan, China
[e] Department of Orthopaedic Surgery, The Third Hospital of Hebei Medical University, China
[f] Key Laboratory of Orthopaedic Biomechanics of Hebei Province, Shijiazhuang, China
[g] Department of Pharmacy, Zhongnan Hospital of Wuhan University, School of Pharmaceutical Sciences, Wuhan University, Wuhan, 430071, China
[h] Hubei Micro-explore Innovative Pharmaceutical Research Co., Ltd, Wuhan, Hubei, 430074, China
[i] Suzhou Organ-on-a-Chip System Science and Technology Co., Ltd, Suzhou, Jiangsu, 215000, China

ARTICLE INFO

Keywords:
Ferroptosis
TRPA1
Diabetes mellitus
Wound healing
Hydrogel

ABSTRACT

Ferroptosis plays a crucial role in the progression of diabetic wounds, suggesting potential therapeutic strategies to target ferroptosis. Transient receptor potential ankyrin 1 (TRPA1) is a non-selective calcium channel that acts as a receptor for a variety of physical or chemical stimuli. Cinnamaldehyde (CA) is a specific TRPA1 agonist. In in vitro experiments, we observed that high glucose (HG) treatment induced endothelial cell ferroptosis, impairing cell function. CA successfully inhibited endothelial cell ferroptosis, improving migration, proliferation, and tube formation. Further mechanistic studies showed that CA-activated TRPA1-induced Ca^{2+} influx promoted the phosphorylation of calmodulin-dependent protein kinase II (CaMKII) and nuclear factor-E 2-related factor 2 (Nrf2) translocation, which contributed to the elevation of glutathione peroxidase 4 (GPX4), leading to the inhibition of endothelial cell ferroptosis. In addition, CA was incorporated into an MMP-9-responsive injectable duplex hybrid hydrogel (CA@HA-Gel), allowing its efficient sustained release into diabetic wounds in an inflammation-responsive manner. The results showed that CA@HA-Gel inhibited wound endothelial cell ferroptosis and significantly promoted diabetic wound healing. In summary, the results presented in this study emphasize the potential therapeutic application of CA@HA-Gel in the treatment of diseases associated with ferroptosis.

1. Introduction

Diabetes mellitus is a chronic metabolic disorder that has the potential to result in a range of severe complications [1]. Diabetic trauma is one of the most severe complications of diabetes mellitus, which not only severely affects the lives of patients but also imposes a heavy economic burden on society [2]. A study suggested that vascular dysfunction due to a localized high-glucose (HG) environment was a

Peer review under responsibility of KeAi Communications Co., Ltd.

* Corresponding author. Department of Pharmacy, Zhongnan Hospital of Wuhan University, School of Pharmaceutical Sciences, Wuhan University, Wuhan 430071, China.
** Corresponding author. Department of Orthopedics, Union Hospital, Tongji Medical College, Huazhong University of Science and Technology, Wuhan, 430022, China.
*** Corresponding authors. Department of Orthopaedic Surgery, The Third Hospital of Hebei Medical University, China.
**** Corresponding author. Department of Orthopaedics, Wuhan Fourth Hospital (Puai Hospital), Wuhan, 430033, China.
E-mail addresses: xiapingfm@163.com (P. Xia), drzyhou@gmail.com (Z. Hou), liuguohui@hust.edu.cn (G. Liu), huhankun@whu.edu.cn (H. Hu).
[1] These authors contributed equally to this paper.

https://doi.org/10.1016/j.bioactmat.2024.09.006
Received 27 June 2024; Received in revised form 20 August 2024; Accepted 4 September 2024
2452-199X/© 2024 The Authors. Publishing services by Elsevier B.V. on behalf of KeAi Communications Co. Ltd. This is an open access article under the CC BY-NC-ND license (http://creativecommons.org/licenses/by-nc-nd/4.0/).

major causative factor in delayed diabetic wound healing, but the specific pathological and molecular mechanisms required further investigation [3].

Ferroptosis is a recently identified form of regulatory cell death characterized by intracellular accumulation of free ferrous ions (Fe^{2+}) and lipid peroxides, which are iron-dependent [4,5]. Recent studies have shown that when fibroblasts and vascular endothelial cells are exposed to high glucose concentrations in vitro, they produce more reactive oxygen species (ROS), lipid peroxidation products, and ferroptosis-associated proteins, which leads to decreased migration and survival [6]. Glutathione peroxidase 4 (GPX4) is crucial in scavenging excess lipid peroxides and is a critical protein in regulating ferroptosis [7]. In the HG environment, the content and activity of GPX4 protein are significantly down-regulated in endothelial cells, leading to an excessive accumulation of reactive oxygen species (ROS) and Fe^{2+}, which are thought to be key triggers of ferroptosis [8]. The Nuclear factor erythroid 2-related factor 2 (Nrf2) plays a significant role in the regulation of cellular redox stability [9]. The progression of diabetic nephropathy can be slowed by the up-regulation of Nrf2, which inhibits the ferroptosis of renal proximal tubular cells [10]. Adipose stem cell-derived exosomes overexpressing Nrf2 can accelerate skin wound healing by improving diabetic wound angiogenesis [11]. A study has demonstrated that Poliumoside prevents type 2 diabetes-associated osteoporosis by inhibiting ferroptosis by activating the Nrf2/GPX4 pathway [12]. However, the effect of ferroptosis on vascular endothelial cells and its role and mechanisms in diabetic wounds need to be further investigated.

The transient receptor potential (TRP) ion channels are a group of channel proteins that are found throughout the central and peripheral nervous systems [13]. TRP channels act as a non-selective calcium channel involved in calcium signaling under physiological conditions [14]. Recent research has provided evidence that TRP channels are present in various types of skin cells, such as melanocytes, keratinocytes, and immune cells. These channels have been demonstrated to have a variety of activities, including skin barrier regulation, hair development, wound healing, inflammation, and itching [15,16]. TRP channels are critical for angiogenesis and other endothelial activities [17]. TRPV1 is involved in simvastatin-activated Ca^{2+} influx in human microvascular endothelial cells, which promotes angiogenesis in vitro [18]. Recent research suggests that TRPV1 reduces M1 macrophage polarisation by triggering Nrf2 nuclear translocation via calcium endocytosis to attenuate osteoarthritis [19]. TRPA1 and TRPV1 have similar cellular depolarizing and calcium influx effects [20]. Cinnamaldehyde (CA), a TRPA1 agonist, has been demonstrated to alleviate the functional impairment of endothelial cells in the presence of high glucose through the activation of Nrf2 [21,22]. The evidence above indicates that TRPA1 may be implicated in diabetic wound healing by inhibiting endothelial cell ferroptosis through the Nrf2/GPX4 pathway.

Hydrogels are a type of wound dressing designed to create a moist environment for wounds, absorb exudates from tissue, and facilitate the delivery of therapeutic drugs to expedite the healing process [23]. Stimulus-responsive drug-loaded hydrogels have garnered significant interest in the biomedical domain in recent years due to their capacity to react to external stimuli [24,25]. The overexpression of matrix metalloproteinase-9 (MMP-9) in wounds is a significant contributing factor that hinders the process of wound healing in individuals with chronic diabetes [26–28]. Gelatin can be degraded in the presence of MMP-9 [29]. HA hydrogels are widely used in bone regeneration, arthritis, and wound healing because of their non-toxicity, good biocompatibility, and injectability [30–32]. Based on the need for diabetic wound healing, we designed an MMP-9 responsive injectable duplex hybrid hydrogel (HA-Gel) with the main components of oxidized hyaluronic acid (HA-CHO) and hydrazide grafted gelatin (Gel-ADH). The hydrogel was mixed with the drug CA and crosslinked into a gel after local in situ injection into the wound site, which was shaped to fit the wound. Then, under the action of MMP-9, gelatin degraded and continuously released CA, which inhibited the ferroptosis of traumatic endothelial cells and accelerated the healing of diabetic wounds.

2. Materials and methods

2.1. Synthesis of oxidized hyaluronic acid (HA-CHO)

Oxidized hyaluronic acid is synthesized using sodium periodate as an oxidizing agent. In this experiment, a total of 2g of sodium hyaluronate (obtained from Shandong Focusfreda Biotech Co., Ltd., China) was introduced into 200 mL of deionized water. Following that, a total of 1.2g of $NaIO_4$ (Aladdin, China) was introduced into the mixture and fully dissolved. The solution was agitated at a speed of 600 revolutions per minute (rpm) at ambient temperature for a duration of 24 h under conditions of low light. Add glycol to neutralize any excess $NaIO_4$. Then, the resultant solution was dialyzed in distilled water over 4 days to eliminate residual $NaIO_4$ and by-products (MWCO: 8–14 kDa). Finally, the product was lyophilized for 4 days and stored at 4 °C for further characterization and usage.

2.2. Synthesis of hydrazide grafted gelatin (Gel-ADH)

In order to synthesize hydrazide-grafted gelatin (Gel-ADH), a mixture containing 2g of gelatin and 2.3012g of adipic acid dihydrazide (ADH, J&K Scientific) was dissolved in 200 mL of morpholine ethanesulfonic acid (MES, J&K Scientific). Following that, 0.5066g of EDC (J&K Scientific) and 0.357g of HOBT (J&K Scientific) were added to the solution. The mixture was subsequently agitated at ambient temperature for a duration of 24 h. The resulting product was subjected to dialysis (molecular weight cut-off 8–14 kDa) against distilled water for a duration of 5 days. Subsequently, the purified Gel-ADH was obtained by freeze-drying.

2.3. Fabrication of the injectable HA-Gel hydrogel

The injectable HA-Gel hydrogel was synthesized by combining equal volumes of HA-CHO and Gel-ADH, which were dissolved in a phosphate-buffered solution, using a dual syringe. In order to generate different concentrations of the injectable hydrogel, the Gel-ADH concentration in the HA-Gel hydrogel was set at a constant value of 16 wt%. By contrast, the concentrations of HA-CHO in the hydrogel were modified to 4 wt%, 6 wt%, and 8 wt%. The cinnamaldehyde (Selleck, China) was added to the Gel-ADH solution before injection.

2.4. Morphology characterization

The HA-Gel hydrogel was rapidly frozen using liquid nitrogen in order to maintain its morphology prior to lyophilization. Following the application of uniform gold spraying, the cross-section images of the HA-Gel were obtained using a scanning electron microscope (SEM).

2.5. Swelling ratio test

The measurement of the hydrogel's swelling rate was conducted using the gravimetric method. The hydrogel was immersed in phosphate-buffered saline (PBS) at a temperature of 37 °C for a duration of 24 h. Subsequently, any extra liquid was removed by gently blotting the hydrogel with filter paper. The hydrogel was then accurately weighed and identified as W_s for labeling purposes. The hydrogel underwent freeze-drying and subsequent weighing and was subsequently designated as W_d. The swelling rate of the hydrogel can be determined using the following formula: swelling rate (%) = $(W_s - W_d)/W_d \times 100$.

2.6. Rheological characterization

The rheological analysis of the hydrogels composed of HA-Gel was

conducted using a TA Discovery-2 Rheometer. The rheometer plates were characterised by a diameter of 20 mm, with a constant gap of 3 mm maintained between them. The rheometer was operated at a temperature of 37 °C. In the time scan test, the strain was maintained at a constant level of 1 % and the frequency was set to 1 Hz. For the subsequent experimental evaluation, the hydrogel samples underwent four cycles in which they were exposed to alternating low strain (1 %, 120 s) and high strain (200 %, 120 s) at a frequency of 1 Hz.

2.7. In vitro degradation

Briefly, degradation assessments were carried out in four distinct solutions: (1) pure phosphate-buffered saline (PBS); (2) PBS containing 25 nM MMP-9; (3) PBS solution with 50 nM MMP-9; (3) PBS solution with 100 nM MMP-9 (n = 3). The initial weight of all samples was documented as W_0. At designated intervals (1, 2, 3, 4, and 5 days), the hydrogel was removed from the solution, excess surface water was eliminated, and the weight was measured and recorded as W_x. The determination of the Gel weight curve was conducted utilising the subsequent formula: Gel weight (% of original) = $(W_x/W_0) \times 100$.

2.8. Cells and cell culture

The Human umbilical vein endothelial cells (HUVECs) were cultured in a controlled environment at a temperature of 37 degrees Celsius and a CO_2 concentration of 5 %. The culture medium was DMEM/F12 (Gibco, USA) supplemented with 10 % fetal bovine serum (FBS, Gibco, USA) and 1 % penicillin-streptomycin mixture.

2.9. RNA sequencing

RNA sequencing was conducted on HUVECs treated with HG or PBS for a duration of 24 h. The extraction of total RNA was performed using the standard TRIzol extraction method provided by Vazyme. The next RNA sequencing was conducted using the Illumina NovaSeq X Plus platform (Gene Denovo Biotechnology Co., Ltd, China). Subsequently, a series of analytical techniques, including heatmap analysis, KEGG enrichment analysis, and GSEA, were employed to investigate the differential expression of genes. A significance level of $p < 0.05$ and a fold change of $\geq$1.5 were used as the criteria for identifying up-regulated and down-regulated genes.

2.10. Western blotting

Total proteins were extracted from HUVECs using RIPA buffer (Beyotime, China) supplemented with 1 % protease and phosphatase inhibitors. Nuclear and cytoplasmic proteins were isolated by Nuclear and Cytoplasmic Protein Extraction Kit (Beyotime, China). The denatured proteins were introduced into a 10 % Omni-Easy™ polyacrylamide gel and subjected to electrophoresis for approximately 60 min when the bromophenol blue (BPB) dye migrated to the bottom of the gel. The gel was subsequently transferred onto a 0.22 μm PVDF membrane (Millipore, Germany) that had been pre-stimulated with methanol. The PVDF membrane was treated with ncmblot blocking buffer (NCM, China) for 15 min. Subsequently, the PVDF membrane underwent three washes with configured TBST. Following this, the primary antibody was introduced into the incubation box and allowed to incubate for a period of 2 h at room temperature. Subsequently, the PVDF membrane underwent three washes with a prepared TBST solution. Following this, a diluted secondary antibody (1:5000) was introduced into the incubation box. The box was then placed in a warped-plate shaker and incubated for a duration of 2 h at a temperature of 25 °C. Finally, the enhanced chemiluminescence process was performed using a Bio-rad Image Capture System.

2.11. RT-qPCR

First, the cell culture medium was aspirated, and sterile PBS was employed to perform two rounds of cell washing. Subsequently, 500 μl of RNA-easy Isolation Reagent (Vazyme, China) was introduced into each well to facilitate the extraction of total cellular RNA. The concentration of RNA was determined using a NanoDrop, and 1 μg of total RNA was utilized for reverse transcription. The cDNA was obtained following reverse transcription and subsequently diluted by adding a 5-fold volume of enzyme-free water. The cDNA, primers, enzyme-free water, and gDNA wiper mix were combined in a 96-well PCR plate following the instructions provided by the SYBR Green Q-PCR Kit (Vazyme, China). The resulting PCR plate was then placed into a BioRad CFX96 instrument for real-time quantitative PCR detection. The primer sequences can be found in Supplementary Table S1.

2.12. JC-1 staining and FCM (flow cytometry) analysis

To assess the mitochondrial membrane potential of HUVECs, the Beyotime JC-1 assay kit was used to evaluate depolarized cells. HUVECs were mixed with the configured JC-1 staining procedure according to the manufacturer's instructions and then placed in a 37 °C cell culture incubator for 20 min. At the end of the incubation, the cells were washed twice with JC-1 staining buffer, stored in an ice bath, and then analyzed by flow cytometry.

2.13. Tube formation assay

Tube formation experiments were conducted using ibidi μ-Slide 15 well (Ibidi, Germany) with a Matrigel matrix (Corning, USA). The HUVECs cell suspension was added to each well at an appropriate density and subsequently incubated for a period of 6–10 h. Images of the area of interest were captured using an optical microscope (Olympus, Japan), and the branching and total branch lengths were quantified using ImageJ (version 1.8.0).

2.14. EdU assay

The EdU test kit (Beyotime, China) was used to perform cell proliferation experiments, following the manufacturer's procedure. More precisely, a solution containing HUVECs was initially introduced into a 96-well plate at a suitable concentration. Subsequently, the cells were cultivated with EdU markers, fixed, rinsed, and made permeable. Subsequently, the EdU reaction was conducted utilising the assortment of chemicals supplied in the kit, while the nuclei were marked with Hoechst 33342, a blue fluorescent dye capable of permeating viable cells. Ultimately, the fluorescence microscope was utilized to obtain equivalent fluorescence images by employing the red and blue channels.

2.15. Transwell and scratching assays

In the transwell migration assay, HUVECs were placed in 24-well transwell chambers (Corning Incorporated, USA) at suitable densities. Then, 1 mL of complete media was introduced to the bottom chamber. Following a 24-h period of co-culture, the chambers were taken out and treated with 4 % paraformaldehyde for fixation. They were then subjected to crystal violet staining, and the migratory cells were captured and quantified using a light microscope (Olympus, Japan).

In the scratching assay, cells were initially inoculated into a six-well plate. Once the cell density reached 95 %, the cells were scratched using a 200ul sterile plastic tip. Following this, the culture was sustained using a low serum medium. Cell migration was captured by an optical microscope at different time points and was quantified by ImageJ (version 1.8.0).

2.16. Cell cycle

HUVECs were inoculated into six-well plates at appropriate density by adding different interventions. After 24 h of intervention, cells were digested with 0.25 % trypsin and collected in 1.5 ml EP tubes, cells were precipitated by centrifugation at about 1000g for 5 min, then 1 ml of ice-bath pre-cooled 70 % ethanol was added and blown to mix, and then stored overnight at 4 °C in a refrigerator. Finally, 0.5 mL of propidium iodide staining solution was added to resuspend the cells and stored at 4 °C in an ice bath. Finally, cell cycle analysis was performed by flow cytometry.

2.17. MDA assay

Malondialdehyde is a natural product of lipid oxidation in organisms, and the Lipid Peroxidation MDA Assay Kit (Beyotime, China) can detect the level of lipid peroxidation. Briefly, HUVECs were lysed with cell lysate, centrifuged to obtain the supernatant, and then placed on ice for temporary storage. Next, the MDA assay working solution and the standards were configured to draw a standard curve. Finally, the recorded absorbance of the sample is graphed in relation to the standard curve to obtain the MDA concentration.

2.18. GSH assay

Intracellular GSH levels were determined using Boyetime GSH and GSSG assay kits. The GSH working solution and standard were prepared according to the manufacturer's instructions. Following the steps in the instructions, the working solution and standards were added to the appropriate cells, and finally the absorbance of A412 was measured with an enzyme marker, and the GSH concentration corresponding to this absorbance was found on the standard curve.

2.19. BODIPY-C11

The lipid peroxidation level of human umbilical vein endothelial cells (HUVECs) was assessed using the BODIPY 581/591C11 kit (Invitrogen, USA). After cell interventions, lipid peroxidation probes were added at a final concentration of 10 μM at 37 °C and for 30 min. Visualization was obtained through a laser confocal microscope (Nikon, Japan).

2.20. Transmission electron microscope (TEM)

The morphological alterations of mitochondria in HUVECs were seen using a transmission electron microscope. Following the treatment of the cells, a 2.5 % glutaraldehyde solution was added to fix the cells, which were subsequently stored in a refrigerator at a temperature of 4 °C for the duration of the night. Subsequently, the cells underwent dehydration, embedding, sectioning, and staining. The mitochondria were visualised using a Hitachi HT-7800 transmission electron microscope (TEM).

2.21. Immunofluorescence

Glass coverslips were placed in 24-well plates and then seeded with a suspension of HUVECs at the appropriate density. The cells were then fixed with 4 % PFA, the membrane was permeabilized with 1 % Triton X-100, and blocked with 10 % goat serum. HUVECs were then incubated with anti-NRF2 (Proteintech; rabbit mAb) primary antibody overnight at 4 °C. Next, they were incubated with anti-rabbit IgG (Proteintech; multi-rAb CoraLite® Plus 488, 1:1000 dilution) secondary antibody for 60 min. The cytoskeleton was then stained with Actin-Tracker Red-Rhodamine (Beyotime, China). Ultimately, the nuclei were dyed with DAPI (Solarbio, China). Images were acquired via a laser confocal microscope (Nikon, Japan).

2.22. Diabetic mouse wound model and treatment

All animal experiments were approved by the Institutional Animal Care and Use Committee of Tongji Medical College, Huazhong University of Science and Technology (HUST). In a brief way, male C57/6J mice that were 8 weeks old were administered intraperitoneal injections of STZ dissolved in 0.1 M citrate-phosphate buffer at a dosage of 50 mg/kg. Blood glucose levels were monitored with blood glucose meters, and diabetes was confirmed when levels exceeded 16.7 mmol/L. Mice were maintained under diabetic conditions for an additional 4 weeks before wounding was initiated. Anaesthesia was initiated with an intraperitoneal injection of 0.3 % pentobarbital sodium at a dosage of 50 mg/kg, which was then followed by the removal of hair from the back. Defect sites were identified and delineated with a pen, and then standardised full-thickness skin wounds (about 1 cm in diameter) were generated along the designated areas using tweezers and fine scissors. The day of wound creation was designated as day 0. Mice were randomly assigned to four groups: DM, DM + CA, DM + HA-Gel, and DM + CA@HA-Gel. Wound surfaces were examined on days 0, 3, 7, 10, and 14.

2.23. Histological analysis

The wound tissue's dermal layer was collected on the 7th and 14th days following the surgery and preserved using a 4 % PFA solution. After dehydration with ethanol, the tissue was embedded in paraffin for sectioning, with a thickness of 4 μm. Subsequently, the specimen underwent staining with H&E and Masson's trichrome for the purpose of tissue examination.

2.24. Statistical analysis

The data were analyzed using IBM SPSS Statistics 22.0 and were given as the mean value plus or minus the standard deviation (SD). The statistical significance of the data was assessed using the Student's t-test and one-way analysis of variance (ANOVA), with a P-value less than 0.05 indicating a significant difference.

3. Result

3.1. The diabetic microenvironment induces endothelial cell ferroptosis in vivo

In order to examine the potential mechanism underlying the process of diabetic wound healing, we developed a mouse model of diabetes by subjecting the mice to a high-fat diet for a duration of 4 weeks and subsequently administering a low dosage of streptozotocin (STZ) via injection. Following this, we proceeded to create a full-thickness wound measuring 1 cm in diameter on the back of the mouse. (Fig. 1A). Wound size was measured on days 0, 3, 7, 10, and 14. As shown in the gross images, wound healing in the diabetes mellitus (DM) group was significantly slower than in the control group (Fig. 1B–C). By day 14, wounds in the DM group had healed to approximately 50 % of their original size, whereas wounds in the control group had completely healed. We also collected wound tissue samples for histologic analysis on days 7 and 14 post-injury. Masson's trichrome staining was used to evaluate the deposition and remodeling of collagen fibers in the wound. As shown in Fig. 1D and G, the DM group showed less collagen deposition and fiber rearrangement than the control group on days 7 and 14. In addition, we used a panoramic view of H&E staining to evaluate wound size in the control and DM groups on days 7 and 14. Similar to the gross wound observations results, the scar widths in the DM group were significantly larger than those in the control group (Fig. 1E and H).

GPX4 is a lipid hydroperoxidase that decelerates lipid peroxidation and is an essential regulator of ferroptosis [33]. MMP9 is a matrix metalloproteinase (MMPs) highly expressed in diabetic wounds [34]. New blood vessel formation, which CD31 marks, plays an essential role

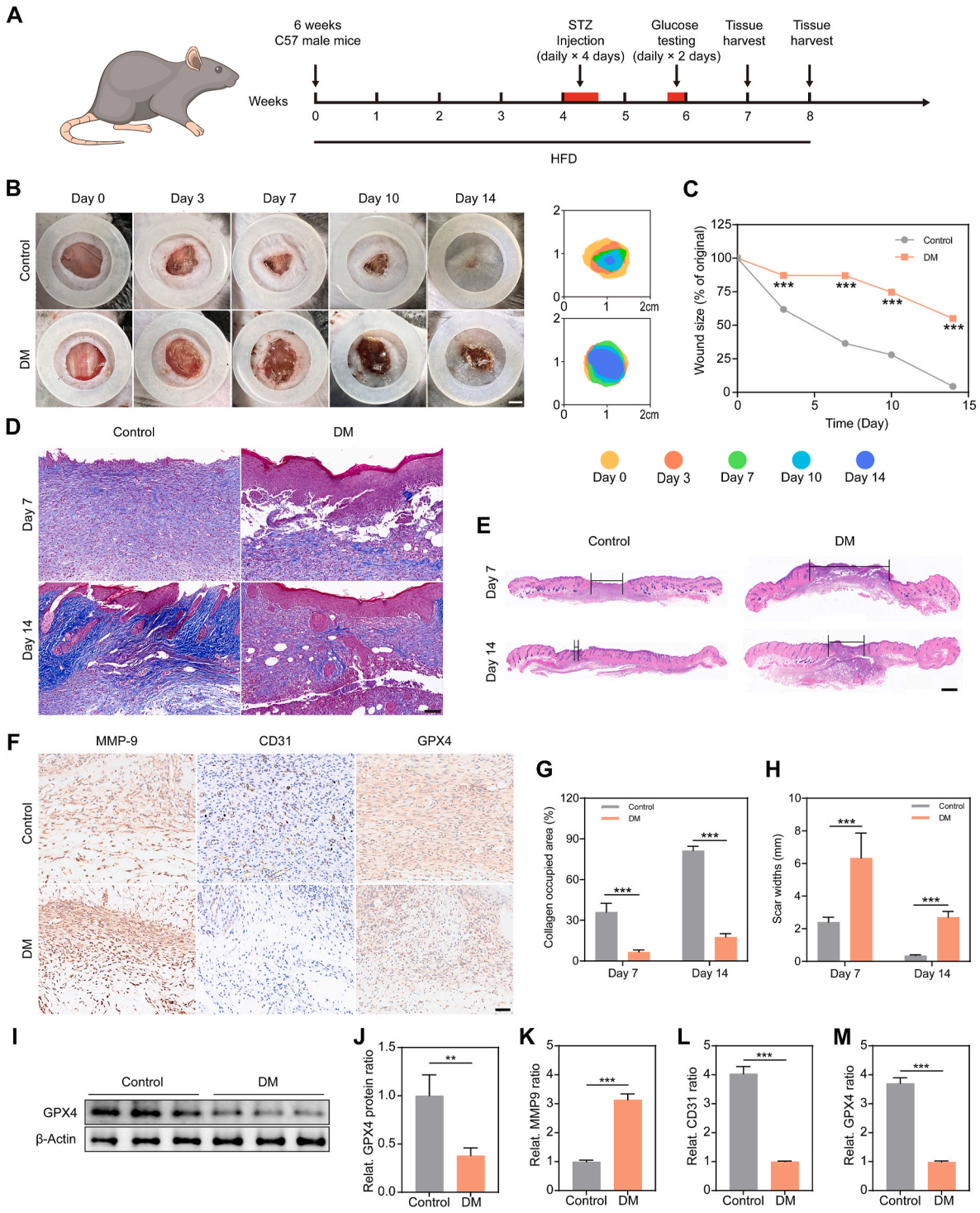

Fig. 1. The diabetic microenvironment induces endothelial cell ferroptosis in vivo. (A) A diagram illustrating the diabetic mellitus model created using a combination of high-fat diet (HFD) feeding and low-dose streptozotocin (STZ) injection. The red squares in the figure indicate the duration of processing. (B) Representative macroscopic pictures of wound healing and closure traces. Scale bar: 2.5 mm. (C) Quantitative analysis of wound closure on days 0, 3, 7, 10 and 14 of control and DM groups. (D) Representative photographs of Masson's trichrome staining and (G) statistical evaluation of collagen-occupied area. Scale bar: 50 μm. (E) A representative panoramic view of H&E staining and (H) quantitative analysis of scar width was used in each group. Scale bar: 1 mm. (F) Representative immunohistochemical images of MMP-9, CD31, GPX4. Scale bar: 50 μm. (I) Western blotting (WB) images of wound tissues with (J) statistical evaluation of the expression level of GPX4. (K–M) Quantitative analysis of immunohistochemistry of MMP-9, CD31, GPX4. The results are shown as the mean ± standard deviation (SD), with a sample size of n = 3. The symbols *P < 0.05, **P < 0.01, and ***P < 0.001. Each group contained three mice.

in wound healing. Here, we performed immunohistochemical (IHC) analysis of GPX4, MMP9, and CD31 in wound tissue. Quantitative analysis revealed an obvious increase in MMP-9 expression and a reduction in GPX4 and CD31 expression in the DM mice (Fig. 1F and K-M). Western blotting (WB) analysis of wound tissue also showed that GPX4 expression was significantly decreased in DM mice (Fig. 1I and J). These findings suggest that the diabetic microenvironment induced local inflammation and ferroptosis of endothelial cells in vivo.

3.2. HG treatment activates ferroptosis and suppresses TRPA1 expression in endothelial cells

To further investigate the molecular mechanism of HG-induced ferroptosis in endothelial cells, RNA sequencing was conducted to identify the genes that exhibited differential expression between the control and HG groups. After 24 h of treatment with HG, a total of 956 genes that exhibited differential expression (fold change >1.5 and P value < 0.05) were identified, of which 483 were upregulated, and 473 were downregulated (Fig. 2A). Furthermore, we conducted an analysis of the RNA sequencing data and carried out pathway enrichment analysis using the Kyoto Encyclopaedia of Genes and Genomes (KEGG) database. As expected, the ferroptosis pathway indicated significant changes based on differentially expressed genes. Surprisingly, we also found differential changes in TRP channels (Fig. 2B). Subsequently, the application of gene set enrichment analysis (GSEA) provided additional evidence that the ferroptosis pathway exhibited significant enrichment and activation. In contrast, TRP channels were significantly enriched but inhibited (Fig. 2C–D). To verify the RNA sequencing results, we performed RT-qPCR. Among the genes related to TRP channels, the expression of TRPA1 was most significantly downregulated (Fig. 2E). High glucose-induced ferroptosis downregulated trpa1 expression in endothelial cells. According to the published literature, activation of trpa1 reversed high glucose-induced endothelial dysfunction [21]. Therefore, we hypothesized that activation of trpa1 could alleviate high glucose-induced endothelial cell ferroptosis.

3.3. TRPA1 alleviates HG-induced ferroptosis in endothelial cells

Cinnamaldehyde (CA) is a specific TRPA1 agonist whose hypoglycemic and hypolipidemic effects have been extensively evaluated in several animal studies [35–38]. We investigated its potential role in HG-induced ferroptosis. To determine the potential toxicity of CA in vitro, we exposed HUVECs to different concentrations of CA solution and found that it was harmless to the cells at CA concentrations up to 100 μM. Furthermore, we examined the effect of CA on HUVECs in HG environment, and our results showed that 30 μM concentration of CA significantly increased the activity of HUVECs. Therefore, we chose this concentration for the following experiments (Fig. S1). Liproxstatin-1 (Lip-1) is a ferroptosis inhibitor that alleviates lipid peroxide accumulation [39]. We used the C11-BODIPY lipid peroxidation probe to characterize the role of TRPA1 in cellular ferroptosis. The C11-BODIPY results showed that endothelial cells exposed to the HG environment exhibited significant lipid peroxidation (fluorescence shifted from red to green), and CA and Lip-1 treatment effectively counteracted this effect (Fig. 3A and J). Glutathione (GSH) and malondialdehyde (MDA) are important indicators of lipid peroxidation [40]. In response to HG stimulation, there was a significant decrease in GSH activity

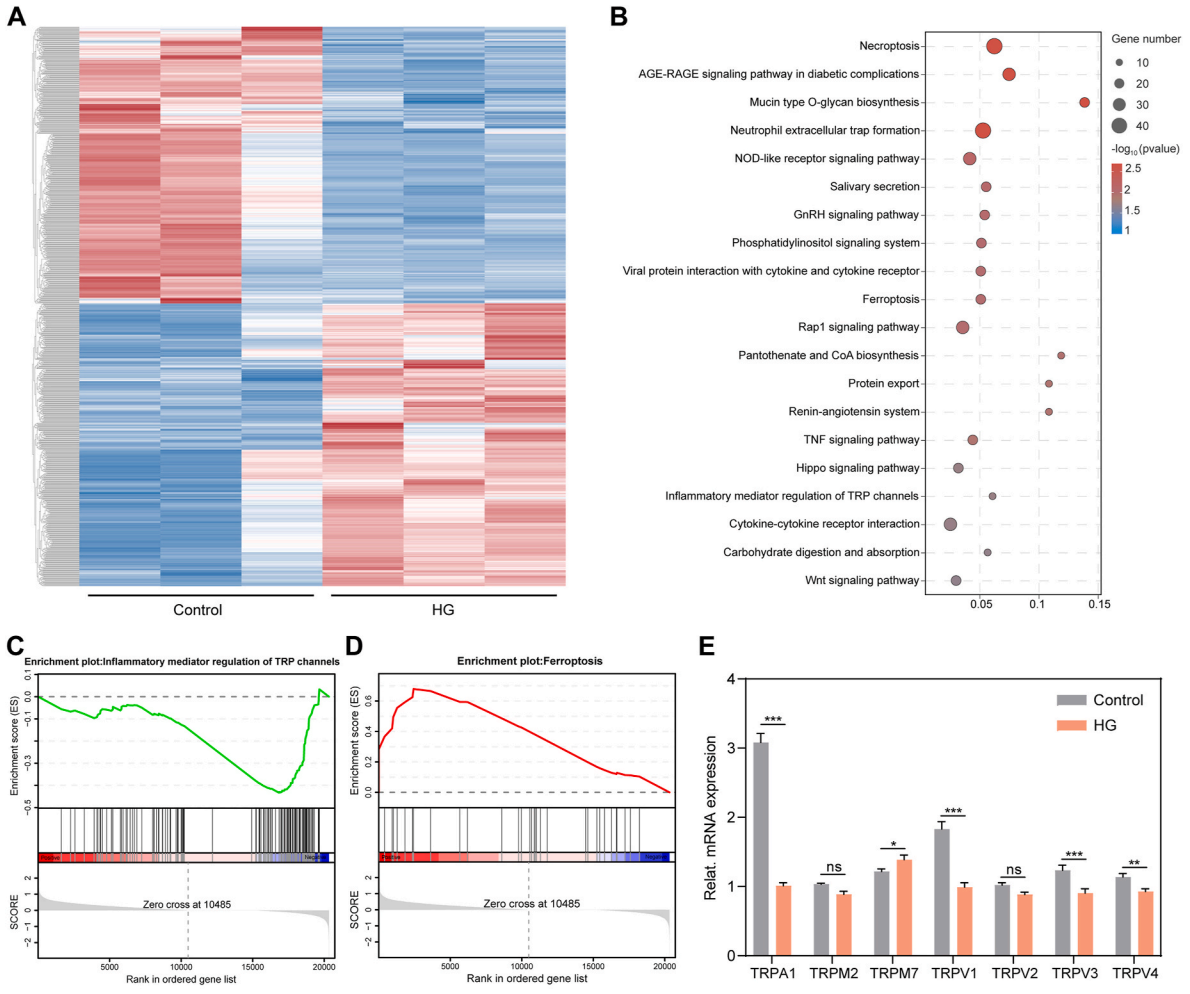

Fig. 2. HG treatment activates ferroptosis and suppresses TRPA1 expression in endothelial cells. (A) Heatmap showing differential gene expression between control and DM groups of HUVCEs. (B) KEGG pathway enrichment analysis. (C) GSEA enrichment score revealed a major reduction in TRP channels in the HG group. (D) GSEA enrichment score revealed significant improvements in the ferroptosis pathway in the HG group. (E) RT-qPCR analysis of TRP channels genes in HUVECs treated with PBS or HG for 24 h. The results are shown as the mean ± standard deviation (SD), with a sample size of n = 3. The symbols *P < 0.05, **P < 0.01, and ***P < 0.001.

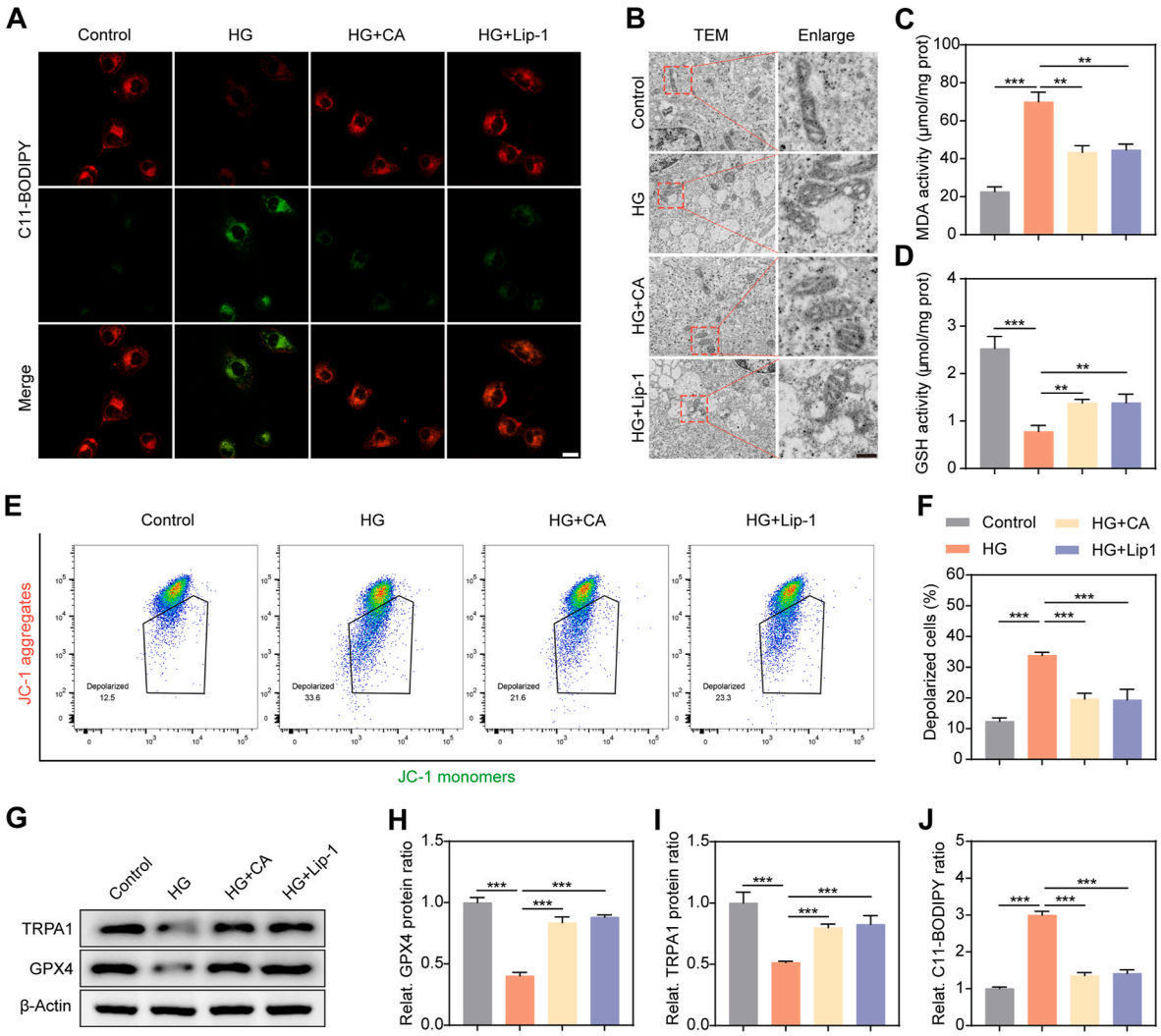

Fig. 3. TRPA1 alleviates HG-induced ferroptosis in endothelial cells. (A) Representative confocal images of C11-BODIPY staining and (J) its quantitative analysis. Scale bar: 20 μm. (B) TEM images of mitochondrial morphology after different interventions. Scale bar: 200 nm. (C) Intracellular MDA levels of HUVECs. (D) Intracellular GSH levels of HUVECs. (E) Depolarized cells labeled by JC-1 staining were observed by flow cytometer. (F) Quantitative analysis of depolarized cells. (G–I) Western-blot images and evaluation of GPX4 and TRPA1 expression in HUVECs. The results are shown as the mean ± standard deviation (SD), with a sample size of n = 3. The symbols *P < 0.05, **P < 0.01, and ***P < 0.001.

accompanied by a marked increase in MDA production, and this change could be reversed by CA and Lip-1 (Fig. 3C–D). Ferroptosis was also accompanied by marked changes in mitochondrial morphology and mitochondrial dysfunction [41]. Transmission electron microscopy (TEM) results showed that mitochondria showed obvious morphological changes (mitochondrial atrophy, reduction or disappearance of mitochondrial ridges, and increase of membrane density) after HG treatment. In contrast, HG-induced mitochondrial morphological changes were alleviated by CA and Lip-1 intervention (Fig. 3B). JC-1 is a probe used to measure the mitochondrial membrane potential. When the mitochondrial membrane potential is high, JC-1 forms aggregates in the matrix of mitochondria. However, when the mitochondrial membrane potential is low, JC-1 remains in its monomeric form and does not aggregate in the matrix of mitochondria. Flow cytometry (FCM) results showed that JC-1 monomer was significantly lower in the CA and Lip-1 groups compared with the HG-treated group (Fig. 3E–F). Finally, further analysis of Western blotting showed that TRPA1 and GPX4 were upregulated in the presence of CA and Lip-1 (Fig. 3G–I). The above results suggested that CA-activated TRPA1 can reverse HG-mediated ferroptosis in endothelial cells.

3.4. TRPA1 alleviates HG-induced dysfunction of endothelial cells

We further investigated the effects of TRPA1 on the proliferation, migration, tube formation, and cell cycle of HUVECs. Our results confirmed that under the influence of HG, EdU-positive cells were significantly reduced, and fewer cells were in the S phase. Interestingly, CA and Lip-1 treatment reversed the HG-induced reduction of EdU-positive cells (Fig. 4A–B), resulting in more cells in the S phase (Fig. 4J–K). The above results indicated an increase in newly synthesized DNA in cells, confirming that CA alleviated the inhibitory effect of HG on cell proliferation. The results obtained from Western blotting analysis also demonstrated that HG treatment led to a decrease in the expression levels of CyclinD1, CyclinD3, and VEGF in HUVECs. Similarly, the HG-induced reduction in protein expression was counteracted by treatment with CA and Lip-1 (Fig. 4C and S2). Subsequently, we found similar results in the scratching assay (Fig. 4D–E) and migration assay (Fig. 4F and H). In addition, the tube formation assay results showed that the CA and Lip-1 groups exhibited more branching and total branch lengths under HG conditions compared with the HG group, suggesting that CA could alleviate the detrimental effects of HG on angiogenesis in HUVECs (Fig. 4G and I). In conclusion, our data emphasized that CA-

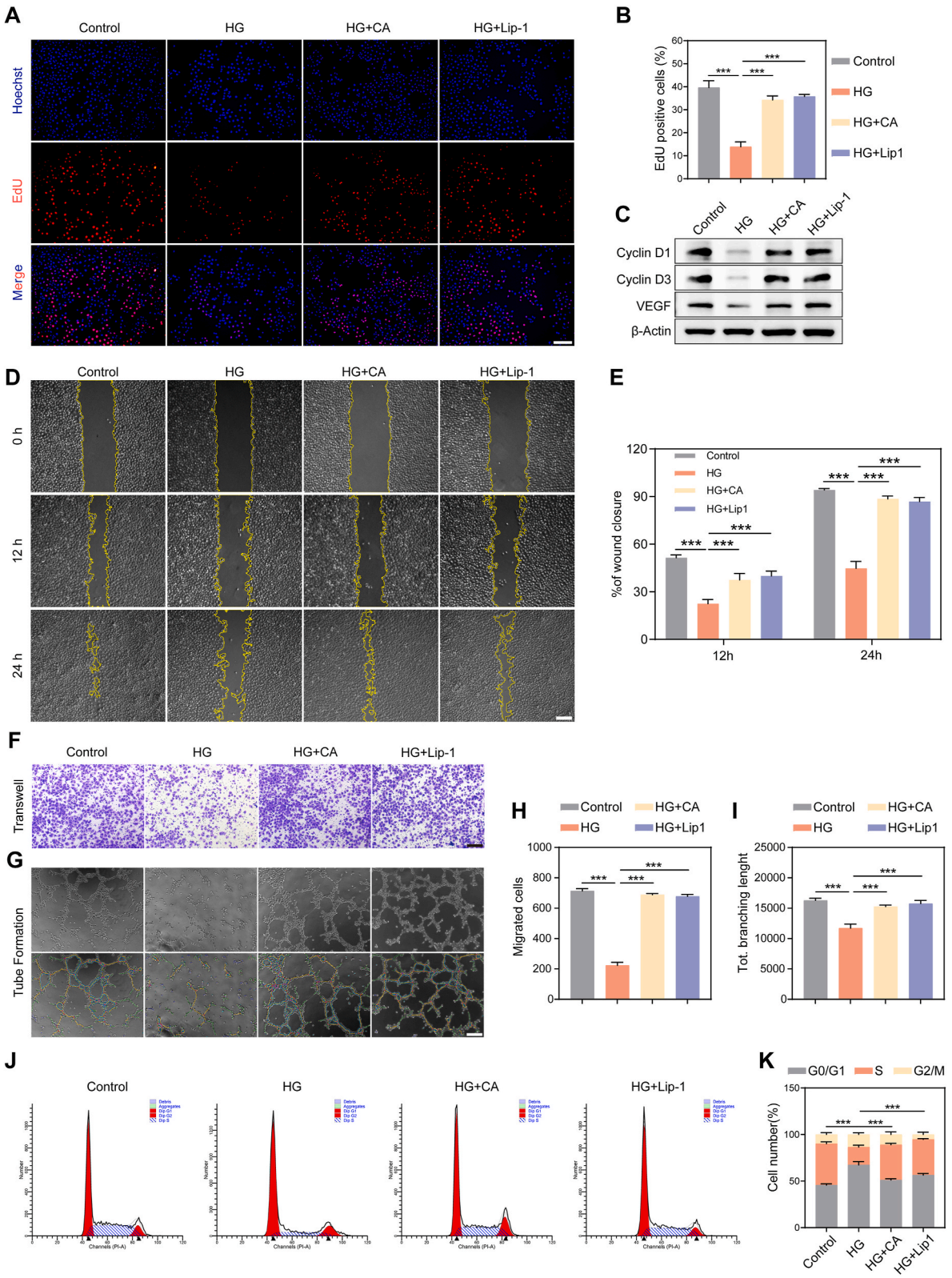

Fig. 4. TRPA1 alleviates HG-induced endothelial cell dysfunction. (A) Representative fluorescence images and (B) statistical evaluation of EdU in HUVECs. Scale bar: 100 μm. (C) Representative WB images of CyclinD1, CyclinD3, and VEGF proteins. (D) Scratching assay and (E) quantitative statistics showing the scratch closure ratio of HUVECs with different treatments. Scale bar: 200 μm. (F) Representative images and (H) corresponding statistical evaluation showing the migrated cells. Scale bar: 100 μm. (G) Results and (I) quantitative analysis of tube formation assays. Scale bar: 100 μm. (J) Flow cytometry (FCM) images of cell cycle distribution, with (K) statistical evaluation. The results are shown as the mean ± standard deviation (SD), with a sample size of n = 3. The symbols *P < 0.05, **P < 0.01, and ***P < 0.001.

activated TRPA1 alleviated HG-induced dysfunction of HUVECs.

3.5. TRPA1 promotes Nrf2 nuclear translocation and inhibits ferroptosis of endothelial cells

The above results prompted us to investigate further how TRPA1 inhibits ferroptosis in HUVECs. The role of Nrf2 in ferroptosis has recently received considerable attention [12,42,43]. Under typical circumstances, the Nrf2 protein is found in the cytoplasm as part of the Nrf2/Keap1 complex. However, when activated, Nrf2 separates from the complex and moves to the nucleus, activating various genes involved in antioxidant and anti-inflammatory responses [44]. Thus, we conducted an investigation into the nuclear localization of Nrf2 subsequent to the activation of TRPA1 using immunofluorescence techniques. In the

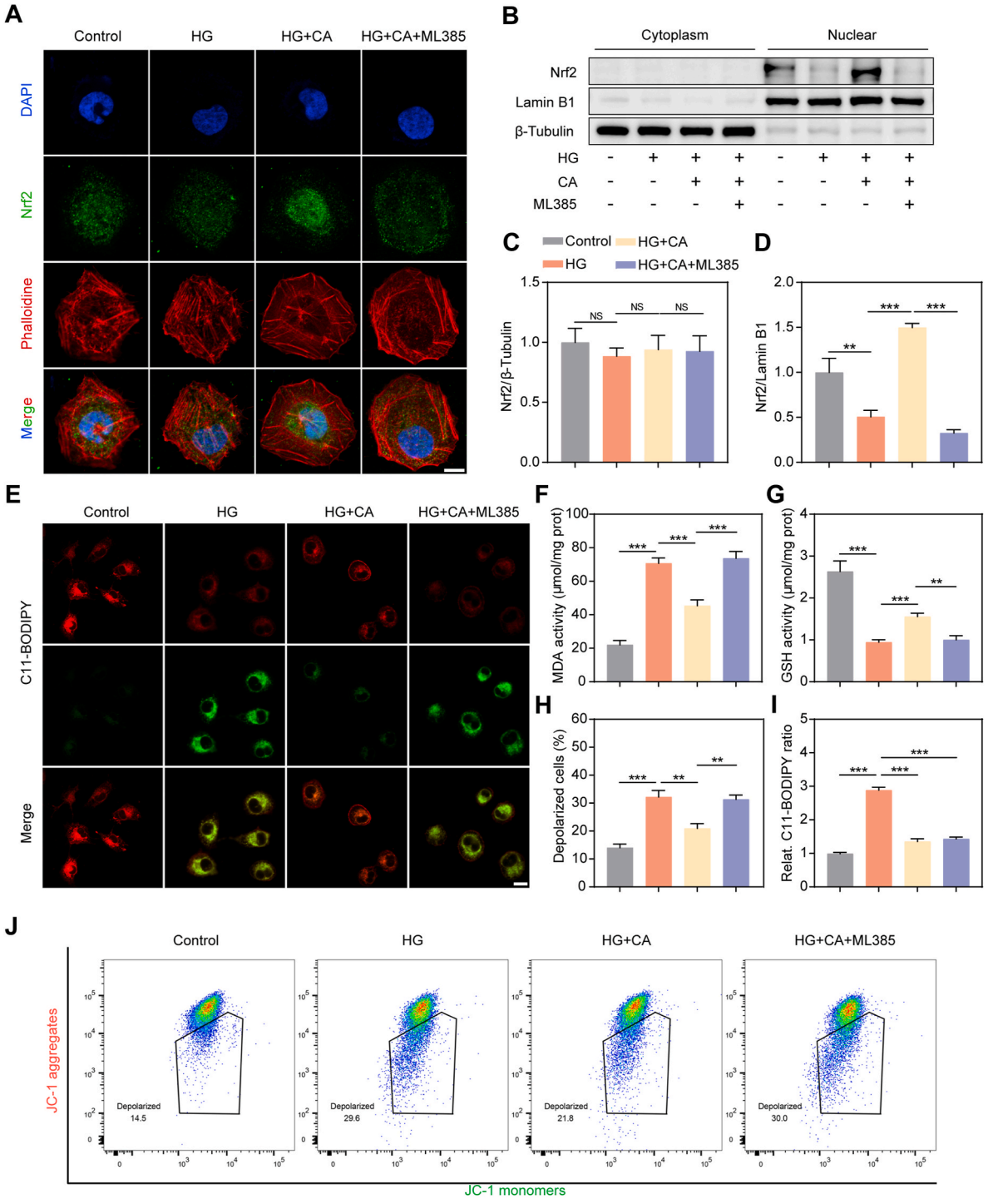

Fig. 5. TRPA1 promotes nuclear translocation of Nrf2 and inhibits ferroptosis of endothelial cells. (A) Confocal immunofluorescence images of Nrf2, cytoskeleton, and nucleus. Scale bar: 10 μm. (B) Western blotting (WB) images and (C–D) quantitative statistics of cytoplasmic and nuclear Nrf2 protein levels in HUVECs. (E) Representative confocal images of C11-BODIPY staining and (I) its quantitative analysis. Scale bar: 20 μm. (F–G) Intracellular MDA and GSH levels of HUVECs. (J) Depolarized cells labeled by JC-1 staining observed by flow cytometer and (H) its quantitative statistics. The results are shown as the mean ± standard deviation (SD), with a sample size of n = 3. The symbols *P < 0.05, **P < 0.01, and ***P < 0.001.

CA-treated group, we observed a significant nuclear translocation of Nrf2 compared to the control and HG groups (Fig. 5A). Analysis of Western blotting results showed a decrease in nuclear Nrf2 in the HG setting. TRPA1 activation induced by CA treatment significantly increased nuclear Nrf2 but not cytoplasmic Nrf2 (Fig. 5B–D), confirming our hypothesis that TRPA1 activation affects Nrf2 nuclear translocation. However, administration of the Nrf2-specific inhibitor ML385 significantly decreased nuclear Nrf2 under TRPA1 activation (Fig. 5A–D). These results suggested that Nrf2 mediates TRPA1 signaling downstream.

Subsequently, an investigation was conducted to determine the necessity of Nrf2 in the inhibition of ferroptosis mediated by TRPA1 in HUVECs.C11-BODIPY results showed that lipid peroxide accumulation by HG treatment could be alleviated by TRPA1 activation through CA treatment, which was partially blocked by ML385 (Fig. 5E and I). The same results were observed in GSH and MDA measurements and flow cytometry of JC-1. (Fig. 5F–H and J). These results revealed the mechanism of action of CA-activated TRPA1, which primarily involved the nuclear translocation of Nrf2, thereby inhibiting ferroptosis in HUVECs. Collectively, these results suggested that TRPA1 activation inhibited ferroptosis in HUVECs through activation of the Nrf2 signaling pathway.

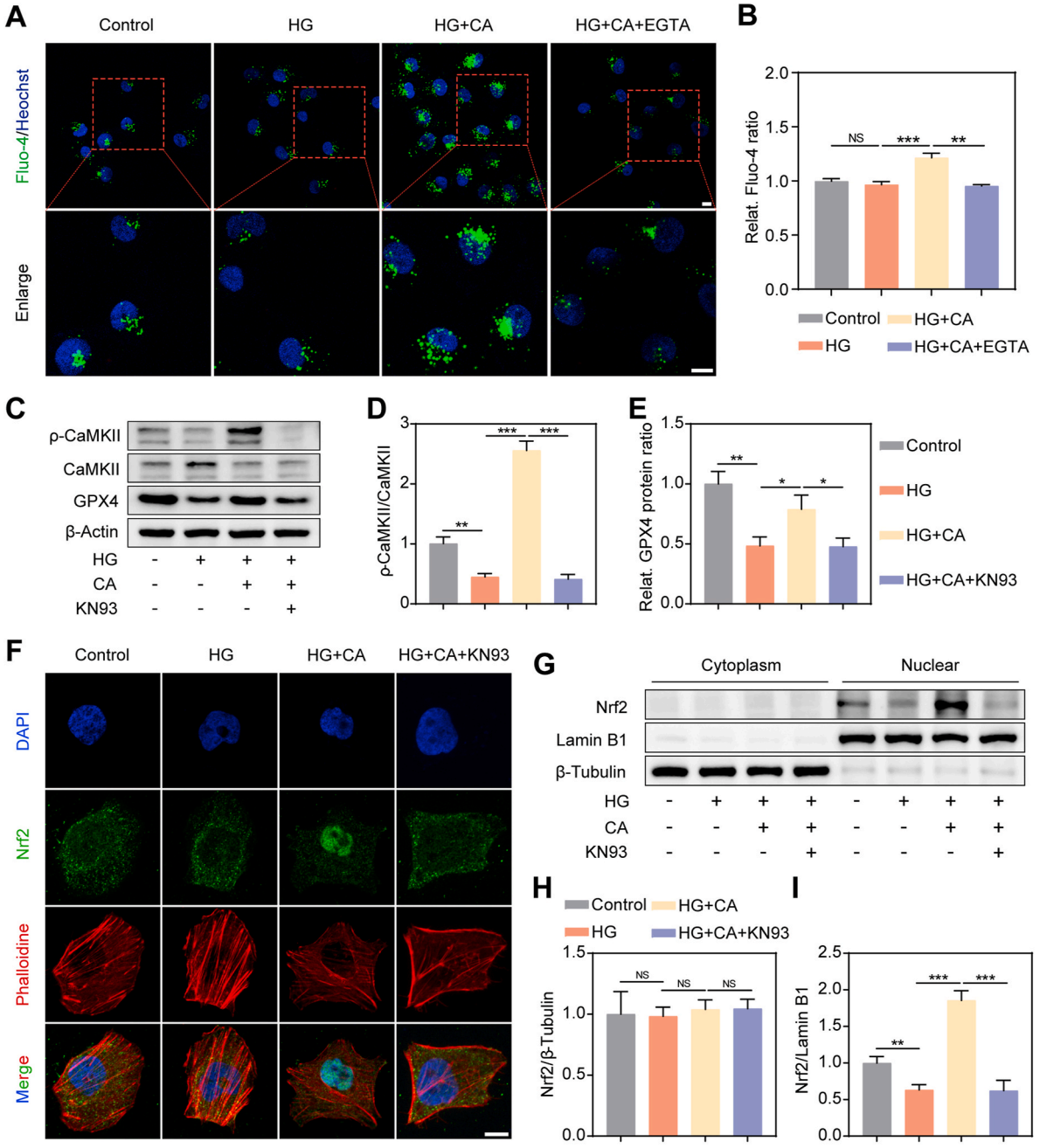

Fig. 6. TRPA1-mediated CaMKII activation facilitates the nuclear translocation of Nrf2. (A) Representative confocal immunofluorescence pictures and (B) quantitative statistics from Fluo-4-stained HUVECs. Scale bar: 50 μm. (C)WB images and (D–E) quantitative statistics of ρ-CaMKII, CaMKII, and GPX4 protein levels in HUVECs. (F) Confocal immunofluorescence images of Nrf2 (green fluorescence), cytoskeleton (red fluorescence), and nucleus (blue fluorescence). Scale bar: 10 μm. (G) Western blotting images and (H–I) quantitative statistics of Nrf2 protein levels of nuclear and cytoplasmic in HUVECs. The results are shown as the mean ± standard deviation (SD), with a sample size of n = 3. The symbols *P < 0.05, **P < 0.01, and ***P < 0.001.

3.6. TRPA1-mediated CaMKII activation facilitates Nrf2 nuclear translocation

As a non-selective calcium channel, TRPA1 provides a pathway for calcium ions (Ca^{2+}) to enter the cell. Calcium ions play a crucial role as second messengers in organisms and participate in a diverse range of cellular signaling pathways [45]. Therefore, we hypothesized that Nrf2 nuclear translocation might be regulated by TRPA1-mediated Ca^{2+} influx. Using the Ca^{2+} probe Fluo-4 AM, we found that CA significantly enhanced the fluorescence intensity of intracellular Ca^{2+}. The intracellular fluorescence intensity was attenuated considerably after using EGTA (a calcium ion chelator), suggesting that CA could activate TRPA1, leading to Ca^{2+} influx. (Fig. 6A–B). CaMKII is a downstream molecule of Ca^{2+} signaling that exerts physiological functions through phosphorylation and participates in various signaling pathways. We hypothesized that CaMKII may mediate signaling between Nrf2 and Ca^{2+}. Western blotting results showed that HG treatment resulted in a decrease in ρ-CaMKII and a significant decrease in the ρ-CaMKII/CaMKII ratio. The ρ-CaMKII/CaMKII ratio was significantly increased by CA treatment, suggesting that CaMKII was activated upon CA treatment. GPX4 showed a similar trend (Fig. 6C–E). KN-93, a competitive inhibitor of ρ-CaMKII, significantly decreased the ρ-CaMKII/CaMKII ratio upon CA activation while significantly decreasing the nuclear translocation of Nrf2 (Fig. 6C and G-I). In addition, the same results were observed in Nrf2 immunofluorescence (Fig. 6F). In conclusion, the above experimental results demonstrated the effect of Ca^{2+}/CaMKII-mediated activation of TRPA1 on Nrf2 nuclear translocation.

3.7. Characterization of HA-Gel hydrogel

CA-activated TRPA1 can restore endothelial cell function by inhibiting ferroptosis. However, local injection of CA is prone to loss and difficult to maintain at the wound site, limiting its clinical application. In order to achieve sustained and effective delivery of CA to the wound, we developed an injectable hydrogel utilising natural hyaluronic acid (HA) and gelatin (Gel) as a carrier for CA. The synthesis of hydrazide-grafted gelatin (Gel-ADH) and oxidized hyaluronic acid (HA-CHO) was carried out, followed by the addition of CA to the Gel-ADH solution. The two

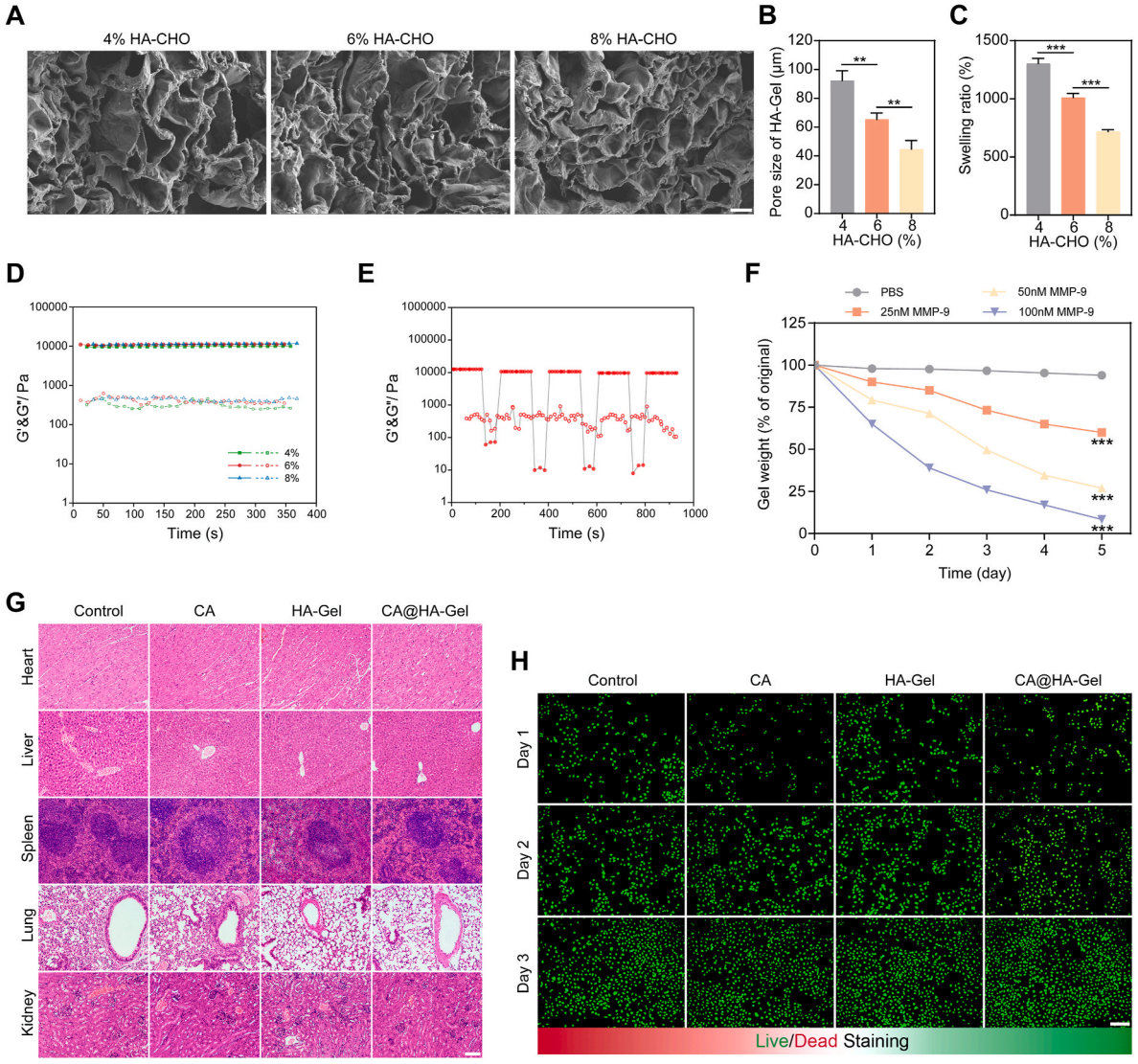

Fig. 7. Characterization of HA-Gel hydrogel. (A) The SEM images, (B) pore size, (C) swelling ratio analysis, and (D) rheological time sweep of HA-Gel hydrogels with a fixed concentration of Gel-ADH (16 %) and the different final concentrations of HA-CHO (4 %, 6 % and 8 %). Scale bar: 100 μm. (E) Shear tinning test of HA-Gel hydrogel (Gel-ADH: 16 % and HA-CHO: 4 %). (F) HA-Gel hydrogel degradation at various MMP-9 concentrations in vitro. (G) In vivo biocompatibility testing for HA-Gel hydrogel. Scale bar: 50 μm. (H) Live and dead staining at 1,2,3 days of HUVECs. Scale bar: 100 μm. The results are shown as the mean ± standard deviation (SD), with a sample size of n = 3. The symbols *P < 0.05, **P < 0.01, and ***P < 0.001.

solutions were then mixed in equal volumes via a dual syringe to form a CA-loaded hydrogel that could be adapted to a variety of wound shapes and sizes. Due to the rapid Schiff base reaction between the hydrazide group of Gel-ADH and the aldehyde group of HA-CHO, our HA gel hydrogel was able to achieve rapid gelation. Subsequently, an examination was conducted to assess the impact of varying concentrations of HA-CHO on the HA-gel hydrogels. Based on the scanning electron microscopy (SEM) images, it is evident that all three groups of HA-gel hydrogels exhibited interconnected porous structures. Furthermore, it can be observed that the density of the pores increased as the concentration of HA-CHO increased (Fig. 7A–B). The swelling ratio experiments showed that the swelling ratio of HA-gel hydrogels decreased as the concentration of HA-CHO increased (Fig. 7C). A high swelling ratio enhances the capacity to absorb wound exudate and guarantees efficient filling of the wound. In addition, we also performed the rheological mechanical test, and the results showed that different concentrations of HA-CHO had no significant effect on the modulus of the HA-Gel hydrogels (Fig. 7D).

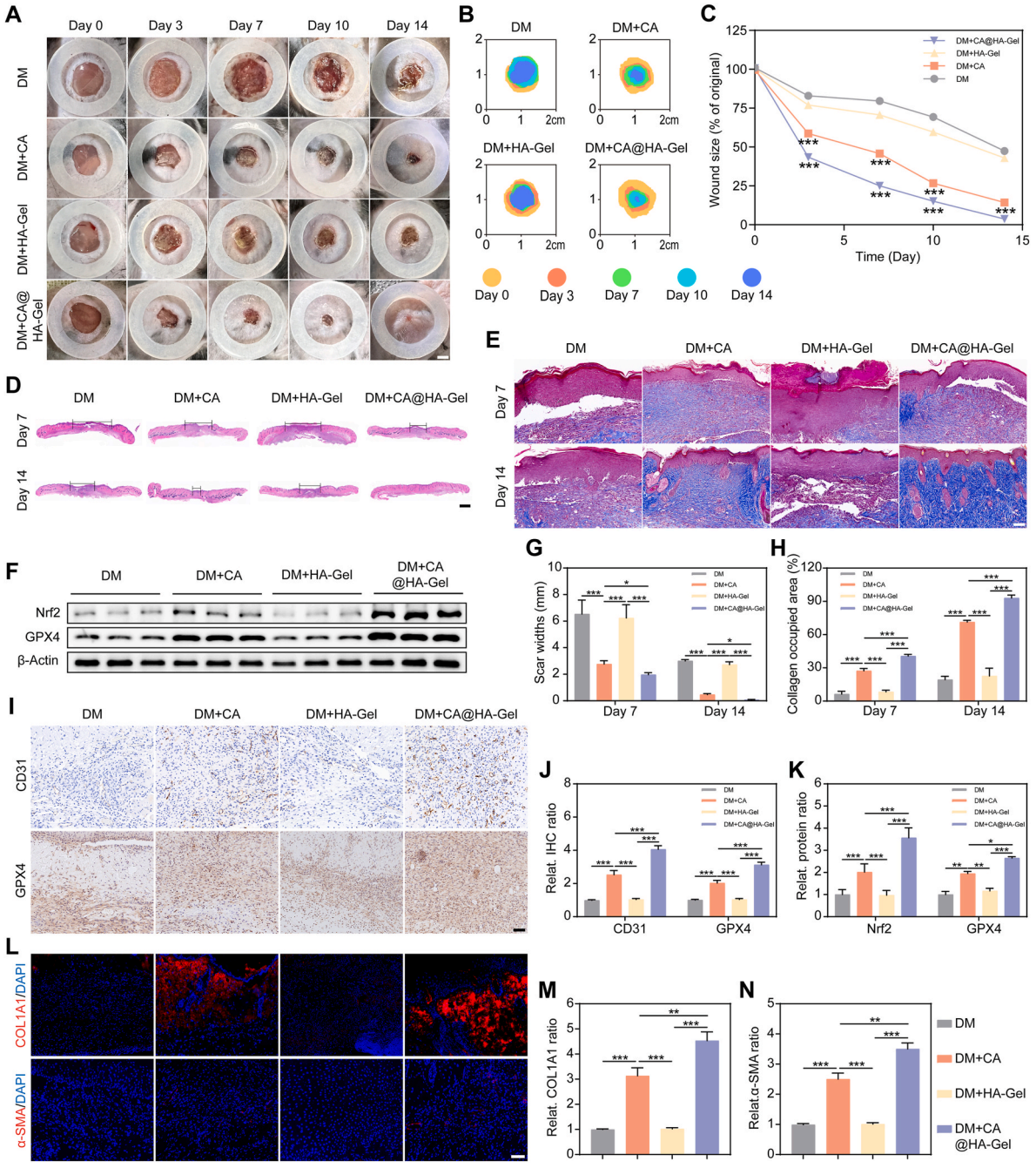

Fig. 8. CA@HA-Gel accelerates diabetic wound healing in vivo. (A) Representative gross images of wound healing and (B) wound closure traces. Scale bar: 2.5 mm. (C) Quantitative statistics of wound closure on days 0, 3, 7, 10, and 14 of DM, DM + CA, DM + HA-Gel, DM + CA@HA-Gel groups. (D) Panoramic view of H&E staining and (G) analysis of scar width in each group. Scale bar: 1 mm. (E) Pictures of Masson's trichrome staining and (H) its quantitative statistics of collagen occupied region. Scale bar: 100 μm. (F) Western blotting images of wound tissue and (K) quantitative statistics of the expression level of GPX4 and Nrf2. (I) Representative immunohistochemistry images of CD31 and GPX4. Scale bar: 50 μm. (J) Quantitative analysis of CD31 and GPX4 immunohistochemistry. (L) Immunofluorescence images and (M–N) quantification of α-SMA (red fluorescence) and COL1A1 (red fluorescence) at wound sites. Scale bar: 100 μm. The results are shown as the mean ± standard deviation (SD), with a sample size of n = 3. The symbols *P < 0.05, **P < 0.01, and ***P < 0.001. Each group contained three mice.

Given this information, we have selected the HA-Gel hydrogel, which is composed of 4 % HA-CHO and 16 % Gel-ADH, as the carrier for the following tests. We tested the shear thinning properties of HA-Gel hydrogels (Fig. 7E). The results showed that the HA-Gel hydrogel could cycle between "high strain" (200 %, G'>G″) and "low strain" (1 %, G'>G″), indicating that the hydrogel had a good self-healing function. Gelatin is a well-defined substrate for matrix metalloproteinases (MMPs). Therefore, we tested the degradation properties of HA-Gel hydrogels in vitro using MMP-9 (Fig. 7F). The findings indicated that even at lower concentrations, MMP-9 had a notable impact on accelerating the degradation rate of HA-Gel hydrogels. Diabetic wounds are often accompanied by excessive local inflammation, so MMP-9-responsive HA-Gel hydrogels degrade faster and continue to release CA.

We then tested the biocompatibility of HA-gel hydrogels in vivo and in vitro. H&E staining showed no histological abnormalities in the heart, lung, liver, spleen, and kidney in the HA-Gel group, indicating that the hydrogel was not significantly toxic (Fig. 7G). We then performed cell live/dead staining of HA-Gel-treated HUVECs or NIH3T3 and found none of the cell morphologies were significantly different (Fig. 7H and S3). Taken together, these results demonstrated that HA-Gel hydrogels had excellent biocompatibility.

3.8. CA@HA-Gel accelerates diabetic wound healing in vivo

Subsequently, we investigated whether CA-activated TRPA1 could accelerate diabetic wound healing in vivo. We created a circular full-thickness skin defect wound (diameter ≈ 1 cm) on the back of diabetic mice with PBS (DM group), CA alone (DM + CA group), and HA-Gel alone (DM + HA-Gel group) as controls. As shown in Fig. 8A–C, wounds treated with CA@HA-Gel (DM + CA@HA-Gel group) were significantly shrunken compared with wounds treated with PBS, CA, and HA-Gel at the time of observation at day 3. At day 14, the area of the wounds treated with CA@HA-Gel was reduced by approximately 95 %, whereas the area of the wounds treated with PBS, CA, and HA-Gel was decreased by only 46 %, 83 %, and 51 %, respectively. In addition, we used H&E-stained panoramas of the wounds on days 7 and 14 to assess the size of the wounds in the different subgroups (Fig. 8D and G). The results showed that in the CA@HA-Gel treatment group, the wound size was reduced to approximately 2 mm on day 7, and the wound was almost completely closed on day 14. These results are consistent with the gross wound healing images, wound closure traces, and quantitative analysis shown in Fig. 8A–C. Next, we stained the wound tissue on days 7 and 14 with Masson's trichrome to obtain high-magnification maps of the wound edges to assess collagen fiber deposition and remodeling. Histological analysis showed that CA@HA-Gel significantly increased collagen fiber deposition in the wound tissue compared with other groups (Fig. 8E and H). Meanwhile, we also took the wound tissues of mice in each group on day 7 for Western blotting, which showed that adding CA significantly increased the expression of Nrf2 and GPX4 proteins (Fig. 8F and K). Immunohistochemical staining of the wounds for GPX4 was consistent with Western blotting (Fig. 8I–J). These results indicated that treatment with CA and CA@HA-Gel inhibited diabetic wound ferroptosis, whereas PBS and HA-Gel did not attenuate diabetic wound ferroptosis. Finally, we collected wound tissues from the 4 groups on day 7 for angiogenesis and collagen deposition assays. We observed that CA@HA-Gel treatment significantly upregulated the expression of CD31, α-SMA, and COL1A1, followed by the DM + CA group (Fig. 8I–J and L-N). These results indicated that CA@HA-Gel treatment could promote neovascularization in diabetic wounds. The aforementioned in vivo experimental findings indicated that the prolonged release of CA of CA@HA-Gel had the potential to enhance the healing of diabetic wounds by suppressing ferroptosis and restoring angiogenesis in wounds.

4. Discussion

The wound healing process is divided into 4 dynamic and overlapping phases: hemostasis, inflammation, proliferation, and remodeling. The process is closely linked to cell migration, proliferation, extracellular matrix deposition and tissue remodeling [46]. A large body of evidence suggested that diabetes has a detrimental effect on wound healing in the form of persistent inflammation of the wound, impaired angiogenesis, delayed healing, and wound infection [3,47–49]. Recent studies have implicated ferroptosis in the pathogenesis of diabetic wounds [6,8,50]. In the present study, we obtained a diabetic mouse model by HFD feeding and low-dose STZ injection. Consistent with these studies, we found that GPX4 expression was down-regulated in diabetic wounds, suggesting the presence of ferroptosis in the wounds. Also, we found delayed healing of diabetic wounds, reduced neovascularization, and less collagen fiber deposition and remodeling.

TRP channels are widely expressed in various types of skin cells [15]. Recent research has indicated that TRP channels have a significant impact on the process of angiogenesis [17,18]. Previous studies have documented that TRPV1 inhibits the polarisation of M1 macrophages by triggering Nrf2 nuclear translocation through the influx of Ca^{2+} [19]. TRPA1 and TRPV1 have similar calcium influx effects [20]. Furthermore, adipose stem cell-derived exosomes overexpressing Nrf2 improved diabetic wound angiogenesis [11]. Several studies have indicated the role of the Nrf2/GPX4 pathway in inhibiting ferroptosis in diabetes-related diseases [12,51,52]. However, the regulatory role of TRPA1 in diabetic wounds, especially on Nrf2/GPX4-mediated ferroptosis in endothelial cells, remains unknown. Our experimental results suggested that TRPA1-induced Ca^{2+} influx enhanced CaMKII phosphorylation, which in turn activated Nrf2 nuclear translocation, leading to upregulation of GPX4, inhibition of ferroptosis in HUVECs, and ultimately reversal of HG inhibition of HUVEC proliferation, migration, and tube formation.

CA, an active ingredient in cinnamon and a TRPA1-specific agonist, is now receiving increasing attention for its role in treating diabetes [53,54]. The standard mode of administration for this type of small-molecule drug is a local injection [12], which makes it difficult to realize its full efficacy due to its rapid clearance. Hydrogel is widely used in tissue repair due to its good biocompatibility [55]. The capacity of responsive hydrogels to react to internal and external stimulus conditions, including biochemical signals and physical stimuli, has garnered significant interest in the domain of tissue repair and regeneration in recent years [24,56,57]. Therefore, we designed an MMP-9-responsive injectable duplex hybrid hydrogel loaded with CA in this experiment. When CA@HA-Gel was applied to diabetic wounds, CA was continuously released by the inflammatory response. The experimental results demonstrated that the hydrogel displayed favorable biocompatibility and effectively suppressed vascular ferroptosis in diabetic wounds, promoting collagen deposition, neovascularization, and wound healing.

5. Conclusion

Collectively, our findings indicate that TRPA1 serves as a significant candidate for the inhibition of endothelial cell ferroptosis in the context of diabetic wound healing. Specifically, CA-activated TRPA1 inhibited ferroptosis of HUVECs through the Ca^{2+}/CaMKII/Nrf2/GPX4 signaling pathway, which enhanced endothelial cell migration, proliferation, and tube formation. Meanwhile, based on the characteristics of diabetic wounds, we designed an MMP-9 responsive injectable duplex hybrid hydrogel as a carrier for CA, which effectively filled different wound shapes and responded to the release of contents. In conclusion, this research offers a promising and novel therapeutic approach to expedite the healing process of diabetic wounds.

Data availability

All data of this study are available within the paper.

Ethic approval and consent to participate

The Institutional Animal Care and Use Committee of the Tongji Medical College, Huazhong University of Science and Technology approved all animal studies (IACUC Number: 2523).

CRediT authorship contribution statement

Chuanlu Lin: Writing – original draft, Conceptualization. **Yiqiang Hu:** Writing – original draft, Investigation. **Ze Lin:** Writing – review & editing, Writing – original draft. **Longyu Du:** Methodology, Investigation, Formal analysis. **Yixin Hu:** Investigation, Formal analysis. **Lizhi Ouyang:** Visualization. **Xudong Xie:** Software. **Peng Cheng:** Data curation. **Jiewen Liao:** Resources, Investigation. **Li Lu:** Validation. **Ruiyin Zeng:** Formal analysis. **Ping Xia:** Resources, Investigation. **Zhiyong Hou:** Validation, Supervision. **Guohui Liu:** Writing – review & editing, Conceptualization. **Hankun Hu:** Writing – original draft, Supervision, Conceptualization.

Declaration of competing interest

Hankun Hu is currently employed by Hubei Micro-explore Innovative Pharmaceutical Research Co., Ltd and Suzhou Organ-on-a-Chip System Science and Technology Co., Ltd. The authors declare that they have no known competing financial interests or personal relationships that could have appeared to influence the work reported in this paper.

Acknowledgments

This work was supported by the National Science Foundation of China (No. 82272491, No. 82072444); Award Program for outstanding recent Ph.D. Graduates at Wuhan Union Hospital (2022) and Hubei Key Laboratory of Regenerative Medicine and Multi-disciplinary Translational Research (2022zsyx009); Chinese Pharmaceutical Association Hospital Pharmacy Department (No. CPA-Z05-ZC-2022-002); Hubei Province Unveiling Science and Technology Projects (No. 2022–35).

Appendix A. Supplementary data

Supplementary data to this article can be found online at https://doi.org/10.1016/j.bioactmat.2024.09.006.

References

[1] H. Sun, P. Saeedi, S. Karuranga, M. Pinkepank, K. Ogurtsova, B.B. Duncan, C. Stein, A. Basit, J.C.N. Chan, J.C. Mbanya, M.E. Pavkov, A. Ramachandaran, S.H. Wild, S. James, W.H. Herman, P. Zhang, C. Bommer, S. Kuo, E.J. Boyko, D.J. Magliano, IDF Diabetes Atlas: global, regional and country-level diabetes prevalence estimates for 2021 and projections for 2045, Diabetes Res. Clin. Pract. 183 (2022) 109119, https://doi.org/10.1016/j.diabres.2021.109119.

[2] D.G. Armstrong, A.J.M. Boulton, S.A. Bus, Diabetic foot ulcers and their recurrence, N. Engl. J. Med. 376 (24) (2017) 2367–2375, https://doi.org/10.1056/NEJMra1615439.

[3] G. Hajmousa, E. Przybyt, F. Pfister, G.A. Paredes-Juarez, K. Moganti, S. Busch, J. Kuipers, I. Klaassen, M.J.A. van Luyn, G. Krenning, H.-P. Hammes, M. C. Harmsen, Human adipose tissue-derived stromal cells act as functional pericytes in mice and suppress high-glucose-induced proinflammatory activation of bovine retinal endothelial cells, Diabetologia 61 (11) (2018) 2371–2385, https://doi.org/10.1007/s00125-018-4713-0.

[4] K. Hadian, B.R. Stockwell, SnapShot: ferroptosis, Cell 181 (5) (2020), https://doi.org/10.1016/j.cell.2020.04.039.

[5] H. Lee, F. Zandkarimi, Y. Zhang, J.K. Meena, J. Kim, L. Zhuang, S. Tyagi, L. Ma, T. F. Westbrook, G.R. Steinberg, D. Nakada, B.R. Stockwell, B. Gan, Energy-stress-mediated AMPK activation inhibits ferroptosis, Nat. Cell Biol. 22 (2) (2020) 225–234, https://doi.org/10.1038/s41556-020-0461-8.

[6] S. Li, Y. Li, Z. Wu, Z. Wu, H. Fang, Diabetic ferroptosis plays an important role in triggering on inflammation in diabetic wound, Am. J. Physiol. Endocrinol. Metab. 321 (4) (2021) E509–E520, https://doi.org/10.1152/ajpendo.00042.2021.

[7] K. Bersuker, J.M. Hendricks, Z. Li, L. Magtanong, B. Ford, P.H. Tang, M.A. Roberts, B. Tong, T.J. Maimone, R. Zoncu, M.C. Bassik, D.K. Nomura, S.J. Dixon, J. A. Olzmann, The CoQ oxidoreductase FSP1 acts parallel to GPX4 to inhibit ferroptosis, Nature 575 (7784) (2019) 688–692, https://doi.org/10.1038/s41586-019-1705-2.

[8] S. Cui, X. Liu, Y. Liu, W. Hu, K. Ma, Q. Huang, Z. Chu, L. Tian, S. Meng, J. Su, W. Zhang, H. Li, X. Fu, C. Zhang, Autophagosomes defeat ferroptosis by decreasing generation and increasing discharge of free Fe2+ in skin repair cells to accelerate diabetic wound healing, Adv. Sci. 10 (25) (2023) e2300414, https://doi.org/10.1002/advs.202300414.

[9] Q. Wang, L. Xu, G. Wang, L. Chen, C. Li, X. Jiang, H. Gao, B. Yang, W. Tian, Prognostic and clinicopathological significance of NRF2 expression in non-small cell lung cancer: a meta-analysis, PLoS One 15 (11) (2020) e0241241, https://doi.org/10.1371/journal.pone.0241241.

[10] S. Li, L. Zheng, J. Zhang, X. Liu, Z. Wu, Inhibition of ferroptosis by up-regulating Nrf2 delayed the progression of diabetic nephropathy, Free Radic. Biol. Med. 162 (2021) 435–449, https://doi.org/10.1016/j.freeradbiomed.2020.10.323.

[11] X. Li, X. Xie, W. Lian, R. Shi, S. Han, H. Zhang, L. Lu, M. Li, Exosomes from adipose-derived stem cells overexpressing Nrf2 accelerate cutaneous wound healing by promoting vascularization in a diabetic foot ulcer rat model, Exp. Mol. Med. 50 (4) (2018), https://doi.org/10.1038/s12276-018-0058-5.

[12] C.-Y. Xu, C. Xu, Y.-N. Xu, S.-Q. Du, Z.-H. Dai, S.-Q. Jin, G. Zheng, C.-L. Xie, W.-L. Fang, Poliumoside protects against type 2 diabetes-related osteoporosis by suppressing ferroptosis via activation of the Nrf2/GPX4 pathway, Phytomedicine 125 (2024) 155342, https://doi.org/10.1016/j.phymed.2024.155342.

[13] A.-P. Koivisto, M.G. Belvisi, R. Gaudet, A. Szallasi, Advances in TRP channel drug discovery: from target validation to clinical studies, Nat. Rev. Drug Discov. 21 (1) (2022) 41–59, https://doi.org/10.1038/s41573-021-00268-4.

[14] A. Paumier, S. Boisseau, M. Jacquier-Sarlin, K. Pernet-Gallay, A. Buisson, M. Albrieux, Astrocyte-neuron interplay is critical for Alzheimer's disease pathogenesis and is rescued by TRPA1 channel blockade, Brain 145 (1) (2022) 388–405, https://doi.org/10.1093/brain/awab281.

[15] M.M. Moran, M.A. McAlexander, T. Bíró, A. Szallasi, Transient receptor potential channels as therapeutic targets, Nat. Rev. Drug Discov. 10 (8) (2011) 601–620, https://doi.org/10.1038/nrd3456.

[16] B.I. Tóth, A. Szallasi, T. Bíró, Transient receptor potential channels and itch: how deep should we scratch? Handb. Exp. Pharmacol. 226 (2015) https://doi.org/10.1007/978-3-662-44605-8_6.

[17] T. Smani, L.J. Gómez, S. Regodon, G.E. Woodard, G. Siegfried, A.-M. Khatib, J. A. Rosado, TRP channels in angiogenesis and other endothelial functions, Front. Physiol. 9 (2018) 1731, https://doi.org/10.3389/fphys.2018.01731.

[18] K.H. Su, S.J. Lin, J. Wei, K.I. Lee, J.F. Zhao, S.K. Shyue, T.S. Lee, The essential role of transient receptor potential vanilloid 1 in simvastatin-induced activation of endothelial nitric oxide synthase and angiogenesis, Acta Physiol. 212 (3) (2014) 191–204, https://doi.org/10.1111/apha.12378.

[19] Z. Lv, X. Xu, Z. Sun, Y.X. Yang, H. Guo, J. Li, K. Sun, R. Wu, J. Xu, Q. Jiang, S. Ikegawa, D. Shi, TRPV1 alleviates osteoarthritis by inhibiting M1 macrophage polarization via Ca2+/CaMKII/Nrf2 signaling pathway, Cell Death Dis. 12 (6) (2021) 504, https://doi.org/10.1038/s41419-021-03792-8.

[20] M.J. Caterina, Z. Pang, TRP channels in skin biology and pathophysiology, Pharmaceuticals 9 (4) (2016).

[21] F. Wang, C. Pu, P. Zhou, P. Wang, D. Liang, Q. Wang, Y. Hu, B. Li, X. Hao, Cinnamaldehyde prevents endothelial dysfunction induced by high glucose by activating Nrf2, Cell. Physiol. Biochem. 36 (1) (2015) 315–324, https://doi.org/10.1159/000374074.

[22] R. Zhu, H. Liu, C. Liu, L. Wang, R. Ma, B. Chen, L. Li, J. Niu, M. Fu, D. Zhang, S. Gao, Cinnamaldehyde in diabetes: a review of pharmacology, pharmacokinetics and safety, Pharmacol. Res. 122 (2017) 78–89, https://doi.org/10.1016/j.phrs.2017.05.019.

[23] C. Hu, F. Zhang, L. Long, Q. Kong, R. Luo, Y. Wang, Dual-responsive injectable hydrogels encapsulating drug-loaded micelles for on-demand antimicrobial activity and accelerated wound healing, J. Contr. Release 324 (2020) 204–217, https://doi.org/10.1016/j.jconrel.2020.05.010.

[24] R. Laurano, M. Boffito, M. Abrami, M. Grassi, A. Zoso, V. Chiono, G. Ciardelli, Dual stimuli-responsive polyurethane-based hydrogels as smart drug delivery carriers for the advanced treatment of chronic skin wounds, Bioact. Mater. 6 (9) (2021) 3013–3024, https://doi.org/10.1016/j.bioactmat.2021.01.003.

[25] F. Qian, Y. Han, Z. Han, D. Zhang, L. Zhang, G. Zhao, S. Li, G. Jin, R. Yu, H. Liu, In Situ implantable, post-trauma microenvironment-responsive, ROS Depletion Hydrogels for the treatment of Traumatic brain injury, Biomaterials 270 (2021) 120675, https://doi.org/10.1016/j.biomaterials.2021.120675.

[26] N. Li, L. Yang, C. Pan, P.E. Saw, M. Ren, B. Lan, J. Wu, X. Wang, T. Zeng, L. Zhou, L.-M. Zhang, C. Yang, L. Yan, Naturally-occurring bacterial cellulose-hyperbranched cationic polysaccharide derivative/MMP-9 siRNA composite dressing for wound healing enhancement in diabetic rats, Acta Biomater. 102 (2020) 298–314, https://doi.org/10.1016/j.actbio.2019.11.005.

[27] R. Lobmann, A. Ambrosch, G. Schultz, K. Waldmann, S. Schiweck, H. Lehnert, Expression of matrix-metalloproteinases and their inhibitors in the wounds of diabetic and non-diabetic patients, Diabetologia 45 (7) (2002) 1011–1016.

[28] T.T. Nguyen, D. Ding, W.R. Wolter, M.M. Champion, D. Hesek, M. Lee, R.L. Pérez, V.A. Schroeder, M.A. Suckow, S. Mobashery, M. Chang, Expression of active matrix metalloproteinase-9 as a likely contributor to the clinical failure of aclerastide in

treatment of diabetic foot ulcers, Eur. J. Pharmacol. 834 (2018) 77–83, https://doi.org/10.1016/j.ejphar.2018.07.014.
[29] J. Liu, Z. Chen, J. Wang, R. Li, T. Li, M. Chang, F. Yan, Y. Wang, Encapsulation of curcumin nanoparticles with MMP9-responsive and thermos-sensitive hydrogel improves diabetic wound healing, ACS Appl. Mater. Interfaces 10 (19) (2018) 16315–16326, https://doi.org/10.1021/acsami.8b03868.
[30] X. Li, X. Chen, L. Guan, W. He, W. Yin, D. Ye, J. Gao, M. Wang, G. Pan, Bioactive metal ion-coordinated dynamic hydrogel with antibacterial, immunomodulatory, and angiogenic activities for infected wound repair, ACS Appl. Mater. Interfaces (2024), https://doi.org/10.1021/acsami.4c05967.
[31] Y. Wang, J. Wang, M. Ma, R. Gao, Y. Wu, C. Zhang, P. Huang, W. Wang, Z. Feng, J. Gao, Hyaluronic-acid-nanomedicine hydrogel for enhanced treatment of rheumatoid arthritis by mediating macrophage-synovial fibroblast cross-talk, Biomater. Res. 28 (2024) 46, https://doi.org/10.34133/bmr.0046.
[32] W. Zheng, L. Ma, X. Luo, R. Xu, Z. Cao, Y. He, Y. Chang, Y. You, T. Chen, H. Liu, Ultrasound-triggered functional hydrogel promotes multistage bone regeneration, Biomaterials 311 (2024) 122650, https://doi.org/10.1016/j.biomaterials.2024.122650.
[33] W.S. Yang, R. SriRamaratnam, M.E. Welsch, K. Shimada, R. Skouta, V. S. Viswanathan, J.H. Cheah, P.A. Clemons, A.F. Shamji, C.B. Clish, L.M. Brown, A. W. Girotti, V.W. Cornish, S.L. Schreiber, B.R. Stockwell, Regulation of ferroptotic cancer cell death by GPX4, Cell 156 (1–2) (2014) 317–331, https://doi.org/10.1016/j.cell.2013.12.010.
[34] W. Zhou, Z. Duan, J. Zhao, R. Fu, C. Zhu, D. Fan, Glucose and MMP-9 dual-responsive hydrogel with temperature sensitive self-adaptive shape and controlled drug release accelerates diabetic wound healing, Bioact. Mater. 17 (2022), https://doi.org/10.1016/j.bioactmat.2022.01.004.
[35] H.M. El-Bassossy, A. Fahmy, D. Badawy, Cinnamaldehyde protects from the hypertension associated with diabetes, Food Chem. Toxicol. 49 (11) (2011) 3007–3012, https://doi.org/10.1016/j.fct.2011.07.060.
[36] S.-C. Lee, W.-X. Xu, L.-Y. Lin, J.-J. Yang, C.-T. Liu, Chemical composition and hypoglycemic and pancreas-protective effect of leaf essential oil from indigenous cinnamon (Cinnamomum osmophloeum Kanehira), J. Agric. Food Chem. 61 (20) (2013) 4905–4913, https://doi.org/10.1021/jf401039z.
[37] W. Zhang, Y.-c. Xu, F.-j. Guo, Y. Meng, M.-l. Li, Anti-diabetic effects of cinnamaldehyde and berberine and their impacts on retinol-binding protein 4 expression in rats with type 2 diabetes mellitus, Chin. Med. J. 121 (21) (2008) 2124–2128.
[38] P. Anand, K.Y. Murali, V. Tandon, P.S. Murthy, R. Chandra, Insulinotropic effect of cinnamaldehyde on transcriptional regulation of pyruvate kinase, phosphoenolpyruvate carboxykinase, and GLUT4 translocation in experimental diabetic rats, Chem. Biol. Interact. 186 (1) (2010) 72–81, https://doi.org/10.1016/j.cbi.2010.03.044.
[39] O. Zilka, R. Shah, B. Li, J.P. Friedmann Angeli, M. Griesser, M. Conrad, D.A. Pratt, On the mechanism of cytoprotection by ferrostatin-1 and liproxstatin-1 and the role of lipid peroxidation in ferroptotic cell death, ACS Cent. Sci. 3 (3) (2017) 232–243, https://doi.org/10.1021/acscentsci.7b00028.
[40] P. Chen, Q. Wu, J. Feng, L. Yan, Y. Sun, S. Liu, Y. Xiang, M. Zhang, T. Pan, X. Chen, T. Duan, L. Zhai, B. Zhai, W. Wang, R. Zhang, B. Chen, X. Han, Y. Li, L. Chen, Y. Liu, X. Huang, T. Jin, W. Zhang, H. Luo, X. Chen, Y. Li, Q. Li, G. Li, Q. Zhang, L. Zhuo, Z. Yang, H. Tang, T. Xie, X. Ouyang, X. Sui, Erianin, a novel dibenzyl compound in Dendrobium extract, inhibits lung cancer cell growth and migration via calcium/calmodulin-dependent ferroptosis, Signal Transduct. Targeted Ther. 5 (1) (2020) 51, https://doi.org/10.1038/s41392-020-0149-3.
[41] Y. Yang, Y. Lin, M. Wang, K. Yuan, Q. Wang, P. Mu, J. Du, Z. Yu, S. Yang, K. Huang, Y. Wang, H. Li, T. Tang, Targeting ferroptosis suppresses osteocyte glucolipotoxicity and alleviates diabetic osteoporosis, Bone Res 10 (1) (2022) 26, https://doi.org/10.1038/s41413-022-00198-w.
[42] M. Dodson, R. Castro-Portuguez, D.D. Zhang, NRF2 plays a critical role in mitigating lipid peroxidation and ferroptosis, Redox Biol. 23 (2019) 101107, https://doi.org/10.1016/j.redox.2019.101107.
[43] A. Anandhan, M. Dodson, A. Shakya, J. Chen, P. Liu, Y. Wei, H. Tan, Q. Wang, Z. Jiang, K. Yang, J.G. Garcia, S.K. Chambers, E. Chapman, A. Ooi, Y. Yang-Hartwich, B.R. Stockwell, D.D. Zhang, NRF2 controls iron homeostasis and ferroptosis through HERC2 and VAMP8, Sci. Adv. 9 (5) (2023) eade9585, https://doi.org/10.1126/sciadv.ade9585.
[44] M. Piotrowska, M. Swierczynski, J. Fichna, A. Piechota-Polanczyk, The Nrf2 in the pathophysiology of the intestine: molecular mechanisms and therapeutic implications for inflammatory bowel diseases, Pharmacol. Res. 163 (2021) 105243, https://doi.org/10.1016/j.phrs.2020.105243.
[45] M. Nazıroğlu, TRPV1 channel: a potential drug target for treating epilepsy, Curr. Neuropharmacol. 13 (2) (2015) 239–247.
[46] M. Wang, X.J.B.T. Wang, Dynamic regulation of the wound repair process: achieving one-stop scar-free repair 5 (2) (2024) 200.
[47] Z. Li, L. Li, M. Yue, Q. Peng, X. Pu, Y. Zhou, Tracing immunological interaction in trimethylamine N-oxide hydrogel-derived zwitterionic microenvironment during promoted diabetic wound regeneration, Adv. Mater. (2024) e2402738, https://doi.org/10.1002/adma.202402738.
[48] C. Yan, J. Chen, C. Wang, M. Yuan, Y. Kang, Z. Wu, W. Li, G. Zhang, H.-G. Machens, Y. Rinkevich, Z. Chen, X. Yang, X. Xu, Milk exosomes-mediated miR-31-5p delivery accelerates diabetic wound healing through promoting angiogenesis, Drug Deliv. 29 (1) (2022) 214–228, https://doi.org/10.1080/10717544.2021.2023699.
[49] D. Lv, X. Cao, L. Zhong, Y. Dong, Z. Xu, Y. Rong, H. Xu, Z. Wang, H. Yang, R. Yin, M. Chen, C. Ke, Z. Hu, W. Deng, B. Tang, Targeting phenylpyruvate restrains excessive NLRP3 inflammasome activation and pathological inflammation in diabetic wound healing, Cell Rep Med 4 (8) (2023) 101129, https://doi.org/10.1016/j.xcrm.2023.101129.
[50] W. Dai, R. Shu, F. Yang, B. Li, H.M. Johnson, S. Yu, H. Yang, Y.K. Chan, W. Yang, D. Bai, Y. Deng, Engineered bio-heterojunction confers extra- and intracellular bacterial ferroptosis and hunger-triggered cell protection for diabetic wound repair, Adv. Mater. 36 (9) (2024) e2305277, https://doi.org/10.1002/adma.202305277.
[51] Z. Gao, Z. Zhang, D. Gu, Y. Li, K. Zhang, X. Dong, L. Liu, J. Zhang, J. Chen, D. Wu, M. Zeng, Hemin mitigates contrast-induced nephropathy by inhibiting ferroptosis via HO-1/Nrf2/GPX4 pathway, Clin. Exp. Pharmacol. Physiol. 49 (8) (2022) 858–870, https://doi.org/10.1111/1440-1681.13673.
[52] Y.-S. Shi, J.-C. Chen, L. Lin, Y.-Z. Cheng, Y. Zhao, Y. Zhang, X.-D. Pan, Dendrobine rescues cognitive dysfunction in diabetic encephalopathy by inhibiting ferroptosis via activating Nrf2/GPX4 axis, Phytomedicine 119 (2023) 154993, https://doi.org/10.1016/j.phymed.2023.154993.
[53] P. Subash Babu, S. Prabuseenivasan, S. Ignacimuthu, Cinnamaldehyde–a potential antidiabetic agent, Phytomedicine 14 (1) (2007) 15–22.
[54] R. Ma, R. Zhu, L. Wang, Y. Guo, C. Liu, H. Liu, F. Liu, H. Li, Y. Li, M. Fu, D. Zhang, Diabetic osteoporosis: a review of its traditional Chinese medicinal use and clinical and preclinical research, Evid Based Complement Alternat Med 2016 (2016) 3218313.
[55] Z. Li, P. Song, G. Li, Y. Han, X. Ren, L. Bai, J. Su, AI energized hydrogel design, optimization and application in biomedicine, Mater Today Bio 25 (2024) 101014, https://doi.org/10.1016/j.mtbio.2024.101014.
[56] J. Fan, E. Pung, Y. Lin, Q.J.B.T. Wang, Recent development of hydrogen sulfide-releasing biomaterials as novel therapies: a narrative review 3 (4) (2022) 250.
[57] W. Chen, H. Zhang, Q. Zhou, F. Zhou, Q. Zhang, J. Su, Smart Hydrogels for Bone Reconstruction via Modulating the Microenvironment, vol. 6, Research (Wash D C), 2023, p. 89, https://doi.org/10.34133/research.0089.